Research Article

Chulin Yu*, Binfeng Liu, Yulin Cui, Wenqing Wang, and Yuxi Yang

# Numerical study on bionic airfoil fins used in printed circuit plate heat exchanger

https://doi.org/10.1515/phys-2023-0200
received September 29, 2023; accepted January 25, 2024

**Abstract:** Airfoil printed circuit heat exchangers (PCHEs) possess exceptional comprehensive performance. In recent years, extensive research has been conducted on the layout and structure optimization of airfoil fins. As biomimetic technologies gradually mature, bionics has achieved numerous outcomes in optimizing airfoil aerodynamic characteristic. Inspired by the sailfish geometry, four types of bionic airfoils are proposed based on the NACA 0015 airfoil, to enhance the thermal-hydraulic performance of the airfoil PCHEs. The results show that while the four types of sailfish airfoils are effective in terms of drag reduction, their overall performance at the same pumping power is suboptimal, with only one type providing an advantage at the low Re region. Moreover, airfoils with concave head curves further increase the weakening of heat transfer by the velocity boundary layer.

**Keywords:** PCHE, bionic, sailfish airfoil, drag reduction

## 1 Introduction

As an essential component in energy conversion systems, the miniaturization of heat exchangers significantly contributes in enhancing the compactness and efficiency of the entire system [1]. Supplemented by advanced manufacturing technology, the printed circuit heat exchanger (PCHE), fabricated through chemical etching and diffusion welding, is characterized by superior compactness and high efficiency, demonstrating substantial tolerance to high temperatures and pressures simultaneously [2]. In this context, as an alternate heat exchanger, PCHE is highly favored in the fourth-generation nuclear power system [3], solar thermal power generation [4], and other fields.

The PCHE was initially proposed and brought to market in 1985 [5], with numerous channel configurations being developed since then. Among the four typical types, namely, straight, zigzag, S-shaped, and airfoil channels, comprehensive research has been undertaken to explore their respective heat transfer and flow friction characteristics [6]. Straight channel PCHEs, lacking spoiler elements, are promising options for applications with low pressure drop requirements. In contrast, the wave-shaped structure of zigzag channels improves the heat transfer performance at the cost of increasing friction loss [7]. Under the premise of retaining heat transfer capacity, the pressure drop in the S-shaped and airfoil PCHEs has improved to varying degrees, amounting to one-fifth [8] and one-twentieth [3] of that in the zigzag channel PCHE, respectively. Consequently, it is demonstrable that airfoil PCHEs showcase superior heat transfer and pressure drop performance.

According to public information, many factors influence PCHE performance, with channel structure being one of the most important [9]. As a result, flow channel design has always been critical to PCHE research and development. Airfoil PCHE has conducted extensive experiments and numerical studies on the local shape and overall layout scale of fins in recent years [10]. Kim *et al.* [11] explored the varying laws in heat transfer and pressure drop performance of the airfoil PCHE under various fin layouts in the S-$CO_2$ integration experiment circuit at the Korea Atomic Energy Research Institute. Additionally, they optimized the geometric arrangement parameters. The heat transfer and pressure drop performance of PCHEs with rectangular, rounded rectangular, elliptical, and airfoil fins were compared by Xu *et al.* [12]. Furthermore, the flow friction characteristics of S-$CO_2$ in channels were analyzed emphatically. According to the numerical results, due to the drastic changes in S-$CO_2$ density with temperature during the flow process, the loss of flow resistance is closely related to the thermal boundary. The impact of three asymmetric airfoil fin layouts on the heat transfer and flow characteristics of PCHEs was discussed by Chu *et al.* [13]. Remarkably, the reverse arrangement of cambered fins,

*** Corresponding author: Chulin Yu,** School of Chemical Engineering and Technology, Hebei University of Technology, Tianjin 300401, China, e-mail: yuchulin@hebut.edu.cn
**Binfeng Liu**, **Yulin Cui**, **Wenqing Wang**, **Yuxi Yang:** School of Chemical Engineering and Technology, Hebei University of Technology, Tianjin 300401, China

compared to the consistent layout, substantially reduces the flow resistance, with a pressure drop of only 22% larger than that observed in symmetrical airfoil channels. Additionally, a hybrid channel structure featuring non-uniform fin layouts was introduced, which increased the thermal-hydraulic performance by an average of 25%. Cui *et al.* [14] changed the cross-sectional shape of the NACA 0020 airfoil fin, and some convex sections of airfoil lines were replaced with concave sections. The local and average thermal-hydraulic properties of two new types of airfoil fin are numerically studied when combined with the fire dissipation number. The new $j$ coefficient increases by 6.15% at maximum due to the thinnest velocity boundary layer. Wu and Xiao [15] extended the 2D airfoil fin profile optimization to 3D structural design. The new fin is made up of two staggered airfoil fins, which is the same as etching airfoil channels on both sides of the plate. Using NACA 0020 airfoil fin as a reference, numerical simulation validates the structure's effectiveness. The results show that turbulent S-$CO_2$ heat transfer is significantly improved, and the overall performance of double-sided etching airfoil PCHE is improved by at least 10.6%. In PCHE airfoil double-sided etching, Xi *et al.* [16] investigated the effect of fin arrangement along the height and flow direction on thermal and hydraulic properties. Even though the volume of the fin is reduced by half by adjusting its height, the fin retains significant application value. Wang *et al.* [17] investigated the effect of asymmetric airfoil shape characteristic parameters (camber, maximum camber position, and thickness) and fin distribution parameters on heat transfer and flow resistance numerically. The boundary conditions are established in accordance with the working conditions of the micro gas turbine regenerator. The results show that the thickness of the airfoil is the most influential factor, and the two most appropriate airfoil shape parameters are also obtained. Jiang *et al.* [18] proposed a machine learning-based optimal design framework for airfoil channel configuration parameters, which avoided the time-consuming problem of a large number of numerical calculations. The impact of geometric parameters such as maximum thickness and location of maximum thickness of airfoil on overall performance is considered. The advanced optimization algorithm improves the performance coefficient of PCHE by about 6.2%. Arora *et al.* [19] established a modular test platform to study the flow friction characteristics of airfoil PCHE, and used the numerical simulation that was strictly verified by the test results to broaden the application range of the correlation of friction coefficient (the Re range was widened from 2,000–25,000 to 100–100,000). Wang *et al.* [17] introduced PSO-BP artificial neural network, and provided a new surrogate model optimization method for airfoil PCHE layout parameters. Using Nu and $f$ as objective functions, the optimal design of fin layout, including horizontal, vertical, and staggered spacing, is obtained. When Nu is basically unchanged, the $f$ coefficient is reduced by about 28%. Inspired by the outline of swordfish, Xu *et al.* [20] first applied the bionic concept to the design of fin in airfoil PCHEs. Based on the original NACA 0020 airfoil, the curve of the trailing edge is mirrored to the leading edge from 50% of the middle arc, and the bionic airfoil with a spindle shape is obtained. The results show that the uniform velocity field of bionic airfoil reduces the pressure drag and the pressure drop of the channel by about 22.8%.

From the literature review, we can see that there has been a lot of work in the structural design and optimization of airfoil PCHE. 2D and 3D designs of fin shape is an effective way to improve PCHE performance. Despite the fact that Xu *et al.'s* research [20] shows that the bionic airfoil fin based on swordfish significantly reduces friction loss. However, bionic design and optimization of airfoil primarily focus on improving aerodynamic characteristics [21], with no attention paid to bionic design of airfoil fin in flow drag reduction and heat transfer enhancement. Sailfish is one of the fastest fish in the ocean, with a top speed of about 110 km/h, indicating that its morphology has excellent hydrodynamic properties. The modified body bone line was applied to the bionic design of spoiler fin in airfoil PCHE based on the design of airfoil fin 2D line and the profile of swordfish. A three-dimensional numerical model is developed to investigate the heat transfer and pressure drop properties of PCHEs with sailfish fins and NACA 0015 airfoil fins. Through analyzing the detouring flow laws of bionic fins and NACA 0015 fins, we explore the flow characteristics and drag reduction mechanism of the sailfish airfoil, and further examine its applicability within PCHEs. The present work serves as a foundational reference for subsequent bionic studies of flow drag reduction in airfoil PCHEs.

# 2 Physical model and numerical method

## 2.1 Bionic design of sailfish airfoils

Using a sailfish specimen made by the research team at Seoul National University in South Korea as the bionic object, four novel bionic airfoils are derived through image processing tools. Figure 1(a) illustrates the side view of the sailfish specimen, showcasing a body length (BL) of 1.74 m, a maximum height to BL ratio of 0.161, and a position of

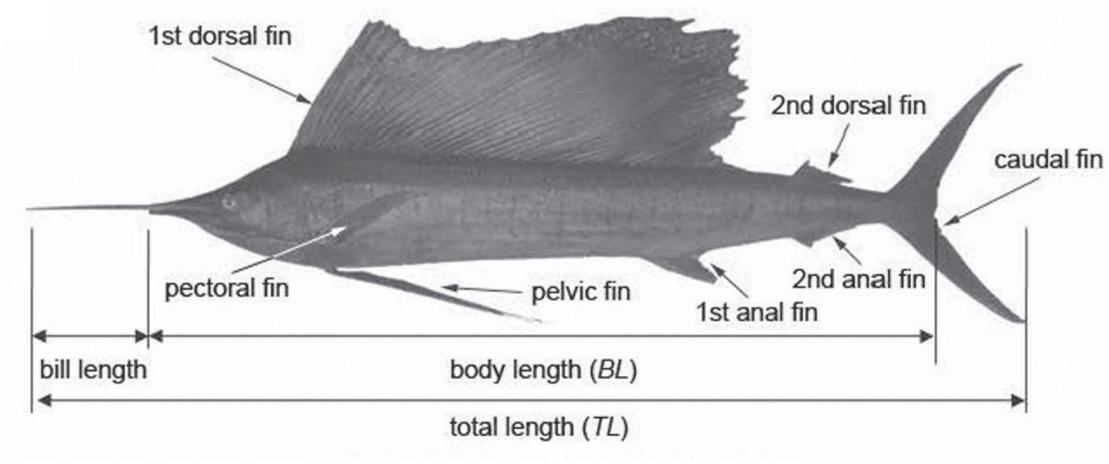


(a)

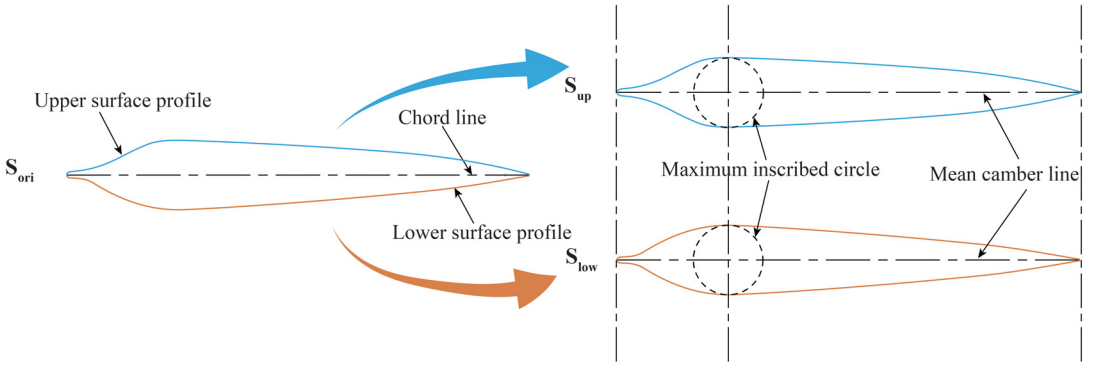


(b)

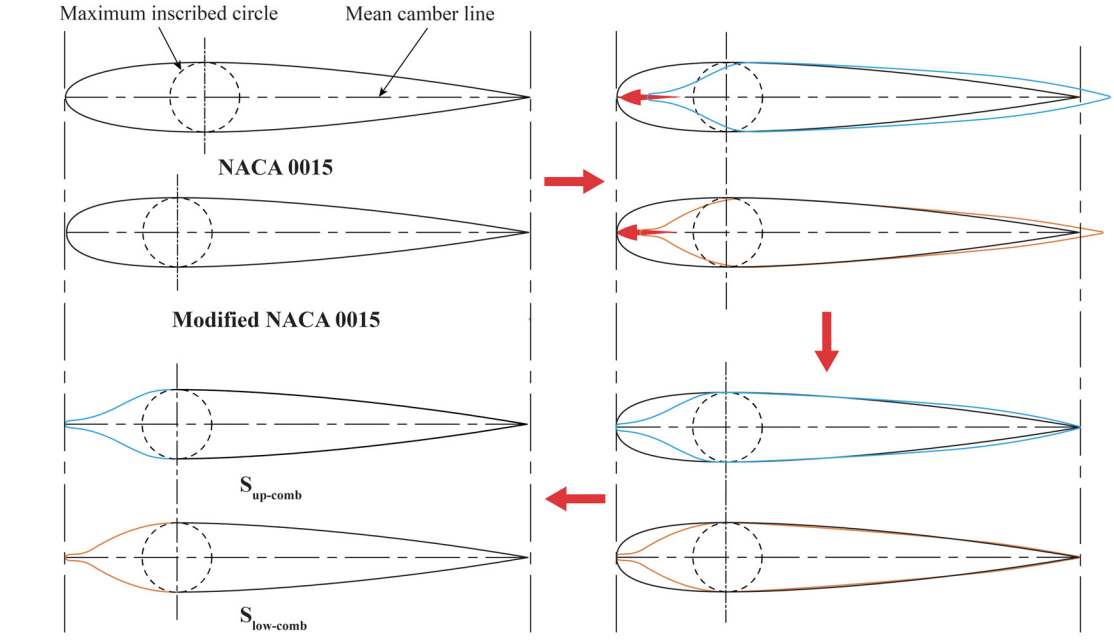


(c)

**Figure 1:** The construction of a geometric model for bionic sailfish airfoils. (a) Overall morphology of the sailfish specimen; (b) symmetric bionic airfoils based on the initial sailfish airfoil; and (c) design of composite sailfish airfoils.

maximum thickness situated at 24% of the BL in the flow direction. For additional detailed parameters, please refer to the study by Sagong *et al.* [22]. The slender bill and expansive dorsal fin are two recognizable morphological features of the sailfish. The protruding upper jaw functions primarily for predation and self-defense [23]. Interestingly, the wind tunnel test conducted on sailfish specimens at an approximate cruising speed of 6.3 km/h demonstrate that the bill does not contribute to drag reduction [22]. The fins serve as the primary organ enhancing body stability and maneuverability during swimming. However, to minimize resistance from an overly expansive wetted area, sailfish retract parts of fins, including the first dorsal fin, the first anal fin, and the abdominal fin, into the fin grooves during coasting.

Based on the above, the side profile curve of the sailfish, with the bill and all fins removed, is selected as the blueprint for bionic airfoil design. The detailed construction process of this geometric model is depicted in Figure 1. Utilizing a third-order spline, the sailfish bone line is extracted, resulting in the initial sailfish airfoil denoted as $S_{ori}$, as shown on the left side of Figure 1(b). Gentle transition treatments are implemented at the intersection of the fins and the bone line to ensure a smooth geometric profile. The fish body's lower jaw tip is designed as the leading-edge point, and the caudal fin is modified into a 0.02 mm diameter arc for modeling and analysis. The midpoint of the tail arc aligns horizontally with the leading-edge point, and the connection between these two points is called chord line. Considering the description and engineering manufacturing issues of the airfoil, a symmetrical structure is typically preferred. Consequently, taking the chord line as the axis of symmetry, the upper (blue line) and lower profile lines (orange line) of $S_{ori}$ are symmetrized to obtain two symmetrical sailfish airfoils, marked $S_{up}$ and $S_{low}$, as depicted on the right side of Figure 1(b). Both schemes maintain a maximum thickness representing 15% of the chord length, with the largest internal tangent circle positioned at 24% of the mean camber line near the leading edge.

The NACA 0015 represents a non-cambered airfoil, characterized by a 15% ratio of maximum thickness to chord length. In this study, the profile line preceding and following the widest position of the airfoil is divided into two parts, called the head and tail profile lines. Based on the NACA 0015 airfoil, we further adapt the $S_{up}$ and $S_{low}$ schemes to obtain two composite sailfish airfoils. As shown in Figure 1(c), the NACA 0015 airfoil is initially modified to shift the maximum inner tangent circle towards the leading edge by 6% of the chord length. Then, with the mean camber lines as a baseline, the modified NACA 0015, $S_{up}$, and $S_{low}$, possessing the same aspect ratio, are placed at the identical horizontal level. The $S_{up}$ and $S_{low}$ schemes are shifted in the direction indicated by the arrows until both the upper and lower surfaces align tangentially with the modified NACA 0015 airfoil. Ultimately, the geometric model undergoes segmentation and reorganizing, linking the tail curve of the NACA 0015 to the head curves of both $S_{up}$ and $S_{low}$. The obtained new airfoils are denoted as $S_{up\text{-}comb}$ and $S_{low\text{-}comb}$, respectively.

## 2.2 Simulation domain and boundary conditions

The core, the primary pressure-bearing component and heat transfer unit of a PCHE, consists of a metal block fabricated through the stacking and welding of etched plates. For airfoil PCHEs, the flow channel formed by the periodically arranged fins is the platform for fluid flow and heat transfer. In this study, the NACA 0015 airfoil is selected as a reference to numerically investigate fins with various shapes used in PCHE.

The simplified PCHE model, comprising two airfoil channels depicted in Figure 2, is identified as an ideal model to significantly reduce the computational and time expenses [24]. The single banked computational model is divided into two distinct areas: the heat transfer section with fins, and the plate extension section devoid of fins. The heat exchanger section houses 20 rows of staggered fins on both the hot and cold side. The inlet extension facilitates full development of the boundary layer, whereas the outlet extension inhibits the effect of the return flow on heat transfer. The incoming flow has an attack angle of 0, progressing from the head to the tail of the fins, with the counter-flow pattern causing the fins on the hot and cold side to face in opposite directions. The sizes of the entire simulation domain are 256.6 mm ($L$) × 2.2 mm ($W$) × 3 mm ($H$), of which the length of the extension segment is 18 mm. Figure 2 demonstrates the geometric parameters of the fin layout, and the supplementary geometric details of the simulation domain are listed in Table 1.

It is noteworthy that, to ensure a meaningful comparison, the dimensional parameters summarized in Table 1 are the same across all types of airfoil fin PCHEs. However, the variations in the shapes among the different types of fins result in discrepancies in the average hydraulic diameter ($D_h$) of the channel. Considering the geometry and arrangement dimensions of the fins, $D_h$ can be written as [25] follows:

$$D_h = \frac{4A_{c,unit}}{A_{s,unit}/L_{unit}} = \frac{4V_{unit}}{A_{s,unit}}, \quad (1)$$

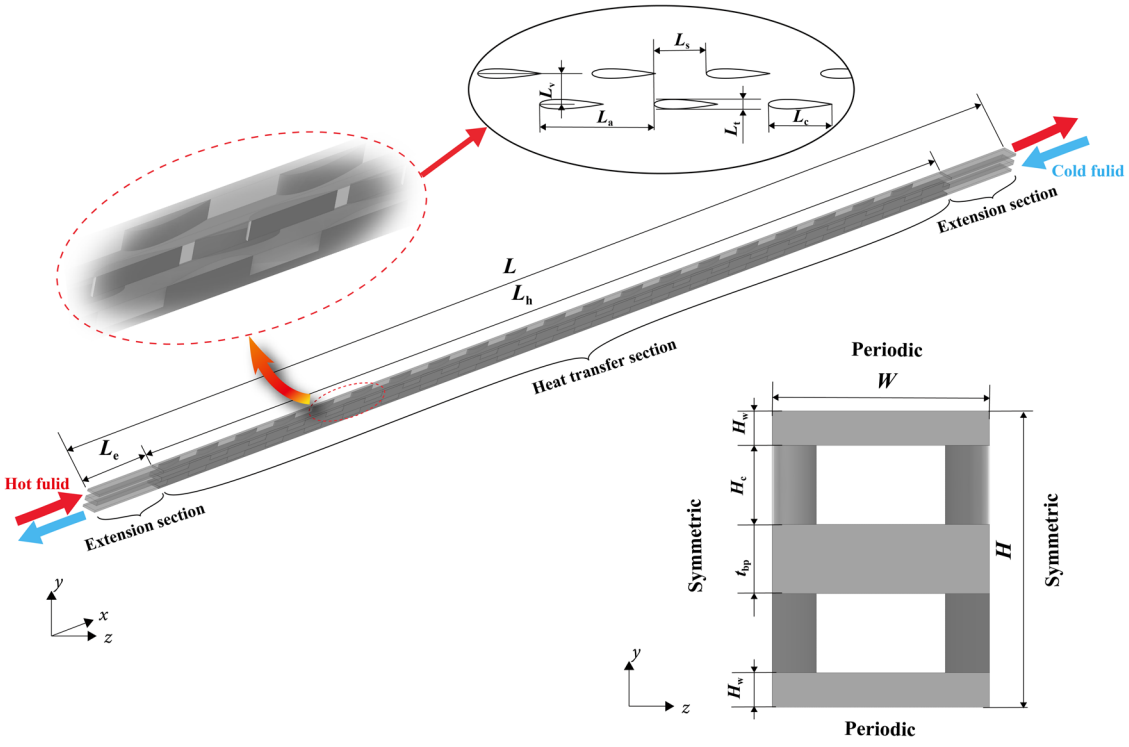


**Figure 2:** Airfoil PCHE simulation domain.

where $V_{unit}$, $A_{s,unit}$, $A_{c,unit}$, and $L_{unit}$ represent the volume, heat transfer area, average cross-sectional area, and length of the minimum periodic heat transfer unit in the fluid domain, respectively. The calculated values for $D_h$ pertaining to the five types of airfoil channels are given in Table 2. It can be seen that the heat transfer area and $D_h$ of the four sailfish fins exceed those of the NACA 0015 airfoil fin. Interestingly, both $S_{up}$ and $S_{low\text{-}comb}$ exhibit identical $D_h$ values and possess the largest heat transfer area.

The setting of boundary conditions is shown in Figure 2. Detailed information about the boundary conditions is as follows:

The fluid domain inlet is subjected to a mass flow rate inlet boundary condition, with the cold and hot fluid inlet temperatures fixed at 292 and 333 K, respectively.

The fluid domain outlet is set as a pressure outlet boundary.

There is no slip between the contact wall surfaces of the fluid domain and the solid domain. The contact wall surfaces of the heat exchange section are set to be coupled.

Apply symmetric boundary conditions on the left and right sides of the computational domain.

Apply periodic boundary conditions to the top and bottom surfaces of the computational domain.

There is no heat flux exchange on the remaining surfaces.

The thermophysical properties of $N_2$, serving as the working fluid in channels, are sourced from the NIST database. Within the investigated range of operating conditions, the density ($\rho$), thermal conductivity ($\lambda$), dynamic

**Table 1:** Geometric information in the simulation domain

| Parameters | Value (mm) | Parameters | Value (mm) |
|---|---|---|---|
| Length of heat transfer section $L_h$ | 220.6 | Longitudinal pitch $L_a$ | 10.8 |
| Length of extended section $L_e$ | 18 | Transverse pitch $L_v$ | 2.2 |
| Height of top and bottom wall $H_w$ | 3.5 | Staggered pitch $L_s$ | 5.4 |
| Height of channel $H_c$ | 8 | Chord length of fin $L_c$ | 6 |
| Thickness of base plate $t_{bp}$ | 7 | Maximum thickness of fin $L_t$ | 0.9 |

**Table 2:** Calculated data for $D_h$ of five airfoil fin channels

| Minimum heat transfer unit for channel | $S_{up}$ | $S_{low}$ | $S_{up\text{-}comb}$ | $S_{low\text{-}comb}$ | NACA 0015 |
|---|---|---|---|---|---|
| Heat transfer area $A_{s,unit}$ ($mm^2$) | 57.996 | 58.328 | 58.328 | 58.268 | 57.712 |
| Volume $V_{unit}$ ($mm^3$) | 16.2 | 16.336 | 16.336 | 16.312 | 16.064 |
| Average cross-sectional area $A_{c,unit}$ ($mm^2$) | 1.5 | 1.513 | 1.513 | 1.51 | 1.487 |
| $D_h$ (mm) | 1.117 | 1.12 | 1.12 | 1.1198 | 1.113 |

viscosity ($\mu$), and specific heat capacity ($C_p$) exhibit a monotonic temperature dependence.

## 2.3 Data reduction and model validation

The thermophysical properties of $N_2$ under an inlet pressure of 3 MPa are presented in Table 3. It can be found that the fluid properties exhibit only minor variations with temperature within the examined operating conditions. Given this, the logarithmic average temperature difference method is employed to calculate the overall heat transfer coefficient ($U$) of the PCHE, as shown in the following equations:

$$U = \frac{Q_{ave}}{A_{s,tot}\Delta T_m}, \quad Q_{ave} = \frac{Q_{hot} + Q_{cold}}{2}, \tag{2}$$

$$\Delta T_m = \frac{(T_{hi} - T_{co}) - (T_{ho} - T_{ci})}{\ln[(T_{hi} - T_{co})/(T_{ho} - T_{ci})]}, \tag{3}$$

where $Q_{ave}$ and $A_{s,tot}$ are the average heat transfer rate and total heat transfer area, respectively, while $\Delta T_m$ refers to the logarithmic average temperature difference. The substitutes h and c represent the fluid in hot and cold sides, respectively; and the substitutes i and o denote the inlet and outlet of the channel on both sides, respectively.

Due to the identical flow channel shape, mass flow rate, and similar working media properties on cold and hot sides, it can be considered that the heat transfer between them has reached a high degree of balance. In other words, the average convection heat transfer coefficients equate for both sides. The total thermal resistance is described as follows:

$$\frac{1}{UA_{s,tot}} = \frac{1}{h_h A_{s,hot}} + \frac{1}{h_c A_{s,cold}}, \tag{4}$$

where $h$ indicates the average convection heat transfer coefficient, and $A_{s,hot}$ and $A_{s,cold}$ are the heat transfer areas for the hot and cold sides, respectively. The thermal resistance method described in the above equation neglects the plate thermal resistance, which was verified in the study by Chung *et al.* [26]. Therefore, the convection heat transfer coefficient on either side can be obtained by the direct method [27] as below:

$$h_h = h_c = \frac{2Q_{ave}}{A_{s,hot}\Delta T_m}, \tag{5}$$

For the evaluation of flow friction and heat transfer characteristics in PCHE, key dimensionless parameters such as the Reynolds number (Re), average Nusselt number (Nu), Prandtl number (Pr), and Fanning friction coefficient ($f$) are defined as follows:

$$Re = \frac{q_m D_h}{\mu A_{c,unit}}, \tag{6}$$

$$Nu = \frac{hD_h}{\lambda}, \tag{7}$$

$$Pr = \frac{\mu C_p}{\lambda}, \tag{8}$$

$$f = \frac{\Delta P}{2u^2\rho}\frac{D_h}{L_h}, \quad u = \frac{q_m}{\rho A_{c,unit}}, \quad \Delta P = P_{in} - P_{out}, \tag{9}$$

where $q_m$ represents the mass flow rate; $u$ indicates the flow velocity; $P_{in}$ and $P_{out}$ correspond to the pressures at the inlet and outlet of the heat transfer section, respectively; and $\mu$, $\rho$, $\lambda$, and $C_p$ are the physical parameters at the mean temperature.

**Table 3:** Thermophysical properties of $N_2$ at cold and hot side inlet temperatures

| Thermophysical properties | 333 K (hot side) | 292 K (cold side) | Difference (%) |
|---|---|---|---|
| $\rho$ (kg $m^{-3}$) | 30.272 | 34.803 | 15 |
| $\mu$ (Pa s) | $1.9761 \times 10^{-5}$ | $1.7984 \times 10^{-5}$ | 9 |
| $\lambda$ (W $m^{-1}$ $K^{-1}$) | $2.9365 \times 10^{-2}$ | $2.644 \times 10^{-2}$ | 10 |
| $C_p$ (J $kg^{-1}$ $K^{-1}$) | 1,078 | 1091.7 | 1.3 |

A performance evaluation criteria (PEC) for PCHE, which considers both thermal and hydraulic performances, is defined as

$$\mathrm{PEC} = \left(\frac{\mathrm{Nu}}{\mathrm{Nu}_{\mathrm{NACA\ 0015}}}\right) \Big/ \left(\frac{f}{f_{\mathrm{NACA\ 0015}}}\right)^{1/3}. \tag{10}$$

With the NACA 0015 airfoil fin as a reference, PEC is used to compare the heat transfer enhancement performance of fins with various configurations at the same pumping power. Consequently, a larger PEC value indicates superior performance. When the value is greater than 1, it indicates that the heat transfer enhancement ratio is greater than the friction enhancement ratio for this fin shape under the same pumping power.

The RNG κ–ε turbulence model is adopted for computational fluid dynamics (CFD) research, combined with enhanced wall functions to reduce the sensitivity of the near-wall grid density. The calculation is performed using the commercial software Fluent, with the target residuals of the continuity equation and the other control equations set to $10^{-3}$ and $10^{-6}$, respectively. Using the PCHE with $S_{up}$ fins as an example, Figure 3 gives the independence verification results for five mesh schemes. To ensure the nodes of the first layer grid to fall within the laminar sub-layer, a five-layer boundary grid with a growth ratio of 1.2 is established, with the $y+$ of the first layer grid always remaining below 5. From the case indicated by the dashed line in the figure, it is observed that numerical results exhibit minimal fluctuations upon grid encryption, with variations in both pressure drop and heat transfer coefficient staying within 1% threshold. Accordingly, the setting method employing a grid count of 9,948,687 is implemented to the mesh system across all examined cases.

A simulation of the NACA 0020 airfoil fin PCHE used in Chung's [26] test is conducted to validate the credibility of the numerical results. As shown in Figure 4, the correlation based on CFD data matches well with that obtained from the experiment results. It is concluded that as the Re decreases, the deviation increases, with a maximum value of 18.4%, a level deemed acceptable for engineering studies.

# 3 Results and discussion

## 3.1 Comparison of thermo-hydraulic performance for different fin configurations

In this subsection, we examine the flow and heat transfer performance of PCHEs with five distinct fin shapes. The corresponding Re range for CFD models with inlet mass flows of 0.13, 0.1975, 0.265, 0.3325, and 0.4 g/s are 5,000–15,500. Notably, the mass flow rates for both cold and hot fluids are maintained to be consistent across all operating conditions.

Figure 5 shows the heat transfer performance and flow resistance of hot channels in PCHEs with five fin configurations. It can be seen that the Nusselt number (Nu) and pressure drop per unit length ($\Delta P/L_h$) are proportional to the Reynolds number (Re). This proportionality can be attributed to the fact that an increase in Re enhances the pulsating effect of turbulence, which in turn intensifies heat transfer and the collisions among fluid microclusters. As shown in Figure 5(a), the Nu among the five configurations

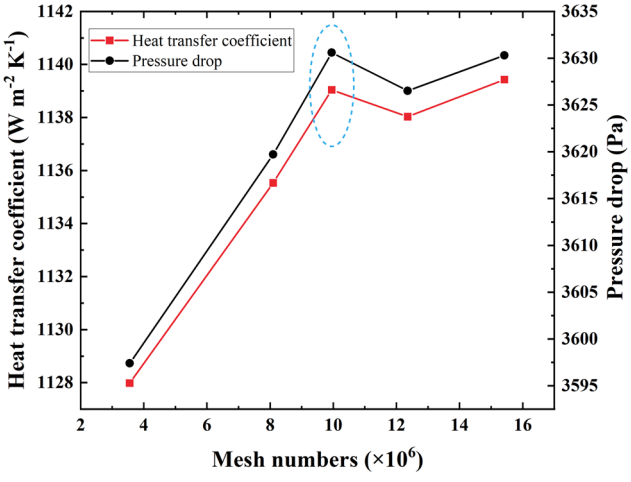


**Figure 3:** Mesh independence test results.

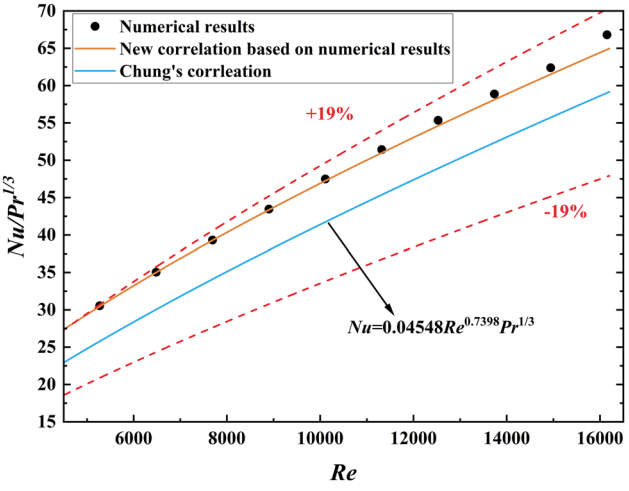


**Figure 4:** Comparison of simulation results with the experimental correlation.

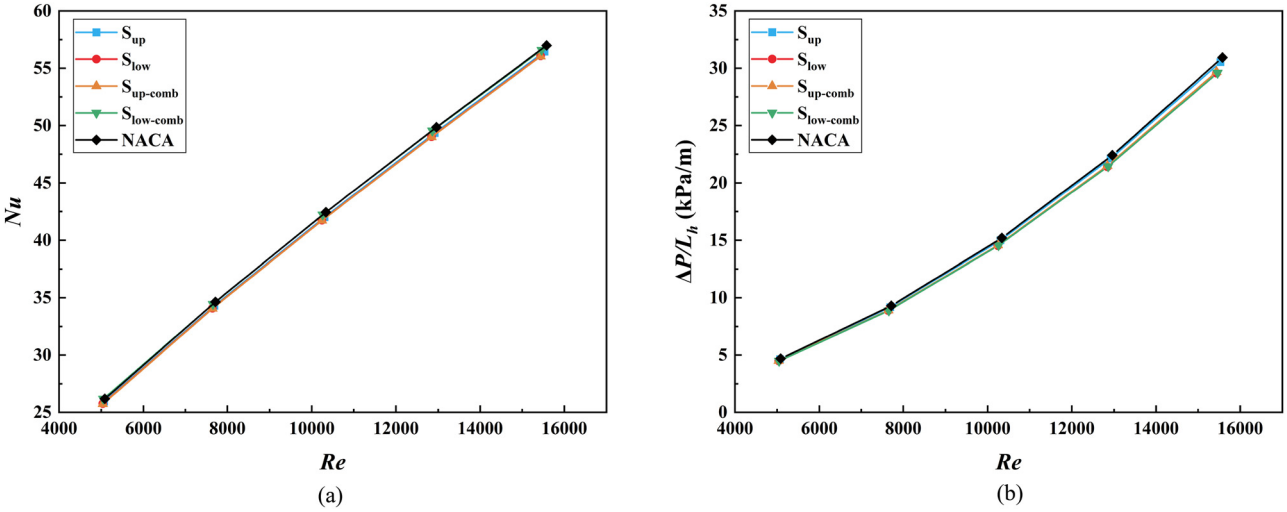


**Figure 5:** Heat transfer and pressure drop performance of PCHEs with bionic and NACA airfoil fins. (a) Nu *vs* Re and (b) $\Delta P/L_h$ *vs* Re.

is quite close to each other, especially at low Re. The greatest discrepancy is a mere 1.74%, occurring between NACA 0015 and $S_{low}$. The Nu of NACA 0015 is marginally higher than the other four sailfish fin types, showing the best thermal performance, while the heat transfer performance of $S_{low\text{-}comb}$ is almost the same as that of NACA 0015. Thus, the bionic fins do not necessarily offer superior heat transfer enhancements. This might be attributed to sailfish fins reducing the fluid disturbances, aligning with the findings from a wind-tunnel test on a sailfish specimen [22], which concluded that the unique outline of the sailfish promotes adherent fluid flow over the majority of its body surface. $S_{low}$ and $S_{up\text{-}comb}$ present the secondary resistance reduction ability compared to that of $S_{low\text{-}comb}$, but better than that of $S_{up}$.

For the pressure drop per unit length ($\Delta P/L_h$), as shown in Figure 5(b), with an increase in Re, the difference in $\Delta P/L_h$ among the various fins becomes more pronounced. It can be seen that NACA 0015 possesses the largest resistance loss, whereas $S_{low\text{-}comb}$ shows the best improvement in pressure drop performance, with an average of 4.4% reduction compared to NACA 0015. This means that the streamlined outline of the sailfish airfoil positively impacts flow resistance reduction. Although Figure 5 indicates that NACA 0015 exhibits superior heat transfer performance, the edge in enhancement is marginal, especially in the case of low Re. $S_{low\text{-}comb}$ has the best hydraulic performance, and meanwhile, its heat transfer performance level is the highest among the four sailfish fins. The performance related to

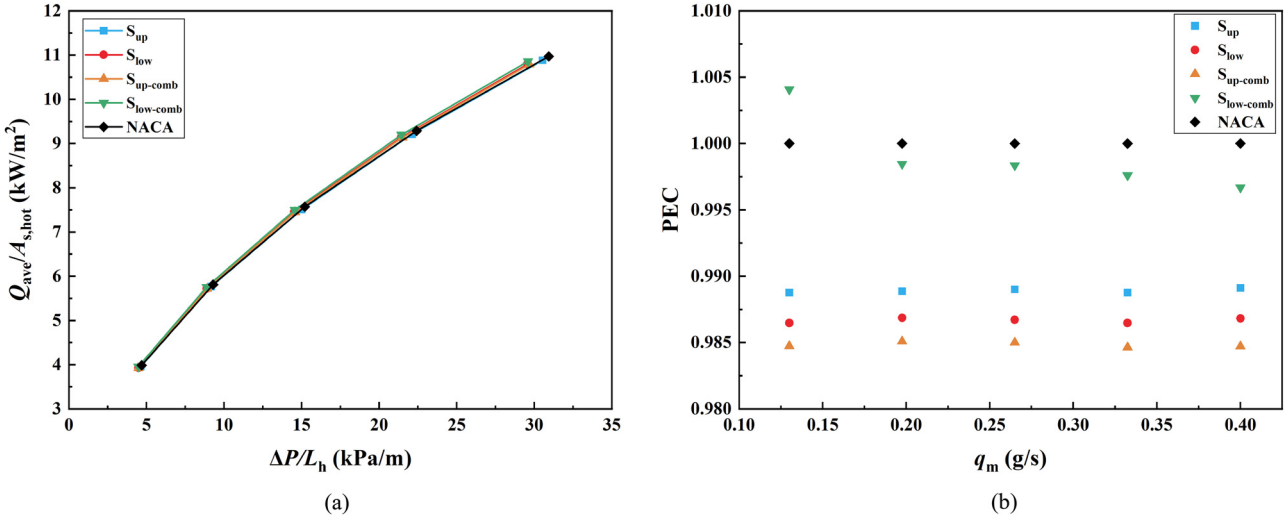


**Figure 6:** Comprehensive performance comparison of PCHEs with bionic and NACA airfoil fins. (a) $Q_{ave}/A_{s,hot}$ *vs* $\Delta P/L_h$ and (b) PEC *vs* $q_m$.

heat transfer and pressure drop for $S_{low}$ and $S_{up\text{-}comb}$ is nearly identical, attributable to their same heat transfer area and hydraulic diameter. Additionally, among the five fins, $S_{up}$ manifests the worst hydraulic performance.

Figure 6 provides a comparison of the overall performance for five types of fins used in PCHE. The ratio of heat transfer rate per unit area ($Q_{ave}/A_{s,hot}$) to pressure drop per unit length ($\Delta P/L_h$) is often employed as a criterion to assess thermo-hydraulic performance and identify the drag reduction capability of various fins in PCHE [28]. Figure 6(a) plots the variation in heat transfer rate per unit area ($Q_{ave}/A_{s,hot}$) with pressure drop per unit length ($\Delta P/L_h$) in the numerical models for five fin types. At the same $\Delta P/L_h$, $S_{low\text{-}comb}$ show the highest while NACA 0015 has the lowest heat transfer performance. According to $\Delta P/L_h$ *vs* Re plot in Figure 5(b), the difference in thermal-hydraulic performance between them becomes more obvious with the increase in Re. This suggests that $S_{low\text{-}comb}$ possesses the best thermal-hydraulic performance among the five fin types, particularly at high $\Delta P/L_h$ resulting from high Re. $S_{low}$ and $S_{up\text{-}comb}$ showcase similar overall performances, slightly better than that of $S_{up}$ and NACA 0015. Combined with Figure 5, it can be found that the higher the flow resistance, the worse the overall performance. Hence, in this study, the contribution of the pressure drop performance to the overall assessment exceeds that of heat transfer performance. In other words, intense turbulence at the expense of high pressure drop does not considerably augment heat transfer, while a weakly turbulent degree of fluid can relatively significantly reduce the drag loss. Although this may slightly decrease thermal performance, it improves the overall performance.

Figure 6(b) demonstrates the comprehensive enhanced heat transfer performance of the five airfoil fin channels at various inlet mass flow rates ($q_m$). Obviously, NACA 0015 serves as the reference fin, its PEC value is always 1. However, Figure 6(b) yields different comparative results compared to Figure 6(a). This discrepancy arises since the $Q_{ave}/A_{s,hot}$ to $\Delta P/L_h$ ratio emphasizes evaluating the effect of flow resistance losses on thermo-hydraulic performance. In Figure 6(b), the PEC values for $S_{up}$, $S_{low}$, and $S_{up\text{-}comb}$ remain below 1, and they all follow similar variation trends, manifesting the insensitivity to $q_m$. Hence, at the same pumping power, $S_{up}$, $S_{low}$, and $S_{up\text{-}comb}$ do not exhibit the heat transfer performance enhancements relative to NACA 0015. The PEC of $S_{low\text{-}comb}$ is only greater than 1 at low mass flow rates, meaning its aptness for applications with either low Re or elevated Re accompanied by low pressure drop requirements.

## 3.2 Flow field analysis in channels with different fins

Figure 7 shows the velocity and pressure fields near the first four rows of fins in the five types of airfoil channels when the inlet mass flow rate is 0.265 g/s. A similar flow behavior around various fin types can be seen from the figure. Primarily, a region of subdued flow velocity is evident near the leading edge of the airfoil, a consequence of flow stagnation stemming from the collision of the fluid with fins. Subsequently, the fluid around the leading edge of the airfoil surface experiences a gradual acceleration owing to the diminishing

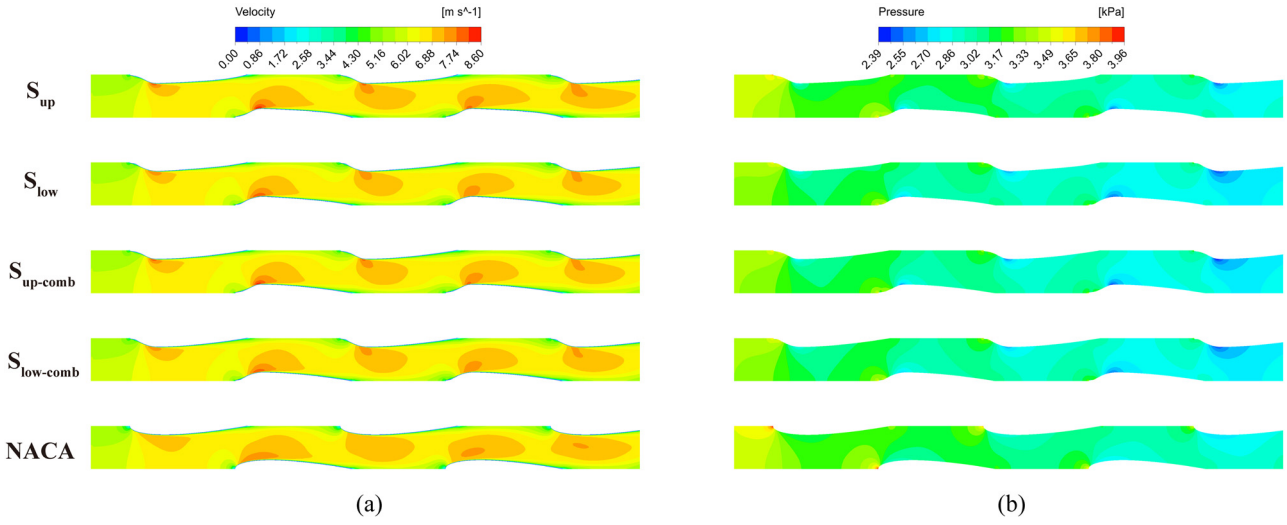


**Figure 7:** Velocity and pressure fields around the first four rows of fins in different types of airfoil channels ($q_m$ = 0.265 g/s). (a) Velocity and (b) pressure.

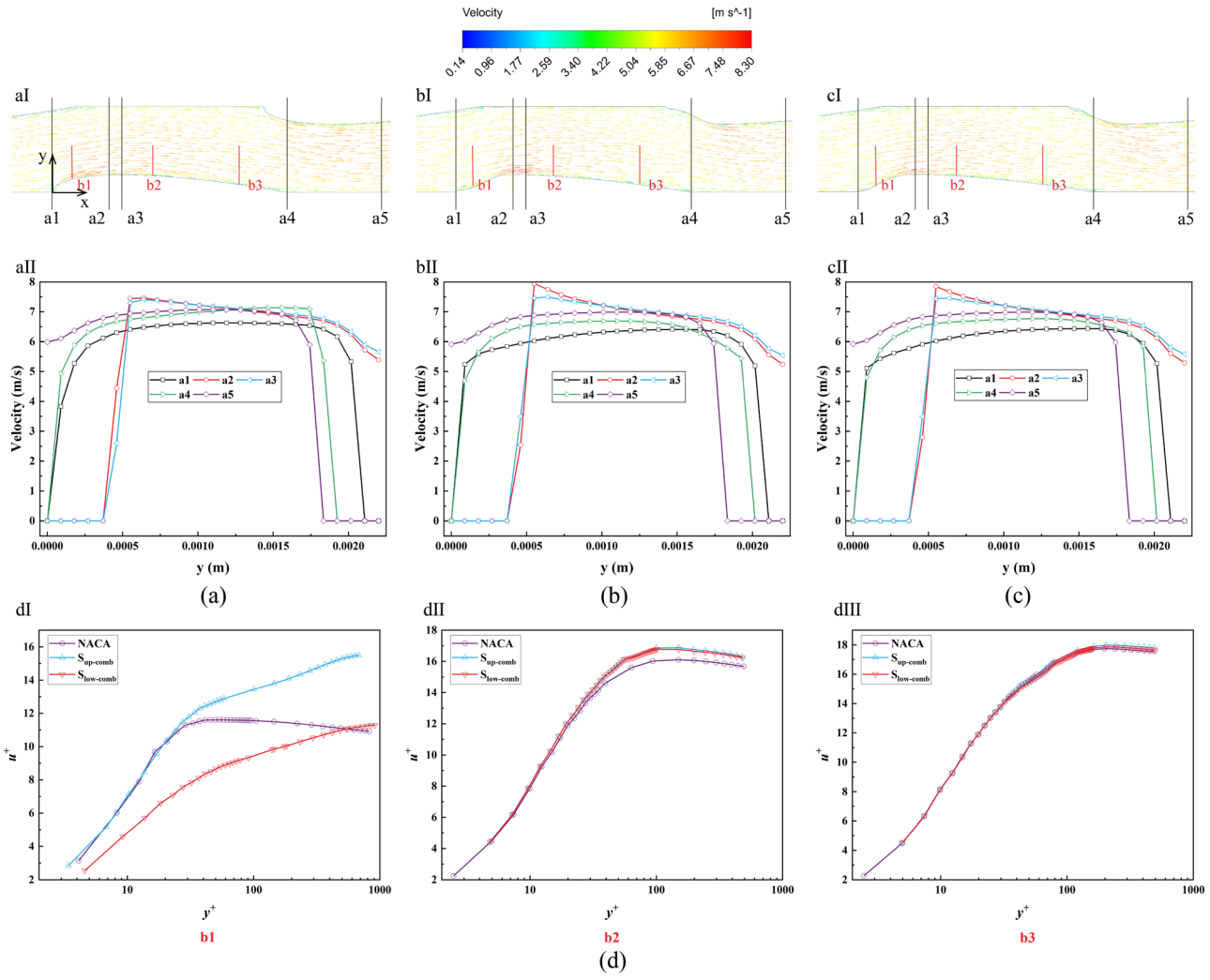


**Figure 8:** Velocity vectors and velocity profiles along the flow direction in channels ($q_m$ = 0.265 g/s). (a) NACA, (b) $S_{up\text{-}comb}$, (c) $S_{low\text{-}comb}$, and (d) Stream wise velocity profiles along b1, b2, and b3 lines.

flow cross-sectional area, culminating at the position near the maximum thickness of the fins. Behind the fins, the separated fluid streams eventually converge, giving rise to a segment of the velocity boundary layer. The flow velocity within the trailing zone is markedly lower compared to that in the main flow area between two neighboring columns of fins.

Variations in fin shapes result in distinct flow fields across different channels. Compared to NACA 0015 configuration, the sailfish airfoils, characterized by their concave leading profiles, expand the fluid domain cross-section along the flow direction. Consequently, these airfoils present a larger low-velocity region near the leading edge, as shown in Figure 7(a), facilitating smaller pressure losses but also simultaneously attenuating heat transfer. Within this context, $S_{low}$, $S_{low\text{-}comb}$, and $S_{up\text{-}comb}$ exhibit analogous extents of low-velocity domain, which are noticeably broader than those seen in $S_{up}$ and NACA 0015. This phenomenon can be attributed to the wider tail of the $S_{up}$ compared to the $S_{up\text{-}comb}$, leading to more contraction of the flow domain along the flow direction from the leading edge under the influence of adjacent columns of fins.

Regions with high flow velocity, located near the widest part of the fins, enhances heat transfer by promoting fluid mixing between the main flow zone and the near-wall surface. However, this also induces an inverse pressure gradient in the flow field. The high flow velocity region compresses the thickness of the velocity boundary layer, causing the dominant flow resistance in this range to switch from viscous friction to differential pressure resistance. As shown in Figure 7(b), the pressure distribution of the sailfish fins is more uniform than that of NACA 0015. Consequently, with the largest area of high-velocity flow region, NACA 0015 presents subpar hydraulic performance, though its heat transfer performance is superior to that of the other four

types of fins. Compared to $S_{low}$ with head profiles featuring shorter concave segments, significant velocity gradients exist in the high-velocity core regions of $S_{up}$ and $S_{up\text{-}comb}$, corresponding to the local low pressure at the same location in Figure 7(b), which is believed to impede heat transfer. Therefore, the velocity vectors and profiles of $S_{up\text{-}comb}$, $S_{low\text{-}comb}$, and NACA 0015 are further analyzed at the second row of fins, as shown in Figure 8. In Figure 8(aI), (bI), and (cI), it is found that different structural flow passages are streamlined without any transverse vortices generated. Combining Figure 7(b), this indicates that the smaller adverse pressure gradient along the flow direction is not enough to cause flow separation on the wing surface, so the flow resistance is mainly generated by friction. Figure 8(aII), (bII), and (cII) show the velocity distribution of three types of wing channel flow fields. It can be seen that at the leading-edge position, the smaller collision area of the biomimetic wing results in a smoother flow field, which is beneficial for reducing flow resistance. By comparing the cross-sections a2 and a3, it is found that the closer the maximum thickness position is to the front, the larger the velocity peak of the fluid flowing along the wall. In addition, in the wing trailing edge and non-wing area, the velocity distributions of the three types of wings are similar, which may be caused by their identical rear shapes. In order to further analyze the boundary layer flow characteristics on the wing surface, the flow velocity profiles at three positions between cross-sections a1 and a2, a3 and a4 are plotted, respectively, ($x/L$ = 0.067, $x/L$ = 0.333, $x/L$ = 0.6), as shown in Figure 8(d). In Figure 8(dI), the boundary layer of the biomimetic wing is obviously thicker than that of the NACA 0015 wing, especially $S_{low\text{-}comb}$. This indicates that the concave curve at the front end of the maximum thickness can smooth the velocity gradient of the wall fluid, reduce the momentum exchange normal to the fluid, and reduce the friction resistance. However, at the same time, due to the increase in the thermal resistance boundary layer, the heat transfer between the fluid and the wall is weakened. In Figure 8(dII), compared with the NACA 0015 wing, the turbulence core velocity of the biomimetic wing is higher. The presence of the boundary layer avoids the momentum exchange between the high-speed mainstream and the wing surface, resulting in drag reduction. In Figure 8(dIII), the boundary layer flow characteristics of the three types of wings are basically the same, therefore, the contribution of the tail of the biomimetic wing to drag reduction is the smallest.

# 4 Conclusion

Inspired by the sailfish, known for its remarkable hydrodynamic properties, we incorporate its silhouette into the spoiler design of an airfoil PCHE, aiming to optimize the airfoil structure and boost the thermo-hydraulic performance of the PCHE. Numerical simulations for four proposed sailfish airfoils and the NACA 0015 airfoil are conducted, with two distinct comprehensive performance evaluation metrics employed for comparison.

The simulations, conducted with $N_2$ as the working medium, reveal that the performance parameters of the five airfoil designs are closely matched. Although the sailfish airfoils have no overall performance advantage over the NACA 0015 airfoil, the drag reduction capability is improved. Among the four sailfish airfoils, $S_{low\text{-}comb}$ has the best thermal and hydraulic performance, with an average pressure drop per unit length 4.4 and 3.2% lower than that of NACA 0015 and $S_{up}$, respectively. Its heat flow density is slightly higher than that of NACA 0015 for the same pressure drop. When the ratio of $Q_{ave}/A_{s,hot}$ to $\Delta P/L_h$ is used as the comprehensive PEC, $S_{low\text{-}comb}$ is superior to NACA 0015, with a maximum difference of 3.5%. When PEC is used as the comprehensive performance assessment criterion, $S_{low\text{-}comb}$ is greater than 1 only at Re = 5,000. Therefore, $S_{low\text{-}comb}$ is suitable for optimizing airfoil structures with low pressure drop requirements, especially under conditions of low flow rate. However, for the examined operating conditions, the PEC values of $S_{up}$, $S_{up\text{-}comb}$, and $S_{low,}$ all below 1, provide a reference for subsequent bionic optimization studies of the airfoil structure.

According to the flow field analysis, no flow separation occurred in all five types of fin walls. The concave curve located in front of the maximum thickness of the airfoil fin helps to increase the velocity boundary layer thickness and reduce the frictional resistance. The more forward the location of the maximum thickness, the greater the peak velocity reached by the wall fluid. The present work provides some methodological guidance for the biomimetic studies of airfoil fins in PCHE. Future endeavors could incorporate the sailfish motion behavior, utilizing 3D reverse engineering for more accurate bionic designs, or developing parametric characterization of airfoils to further optimize the airfoil structures for improving performance.

**Acknowledgments:** This work is supported by the National Natural Science Foundation of China (52106086) “Mechanism of heat transfer enhancement and flow drag reduction of bionic high temperature microchannel plate heat exchanger with synergetic effect of force, flow and temperature” for which authors would like to express their sincere thanks.

**Funding information:** Project supported by National Natural Science Foundation of China Mechanism of heat transfer enhancement and flow drag reduction of bionic high

temperature microchannel plate heat exchanger with synergetic effect of force, flow and temperature (No. 52106086).

**Author contributions:** Chulin Yu: conceptualization, funding acquisition, writing – review, and methodology. Binfeng Liu: investigation, resources, data simulation, and writing – original draft. Yulin Cui: data curation and visualization. Wenqing Wang: data simulation. Yuxi Yang: data processing. All authors have accepted responsibility for the entire content of this manuscript and approved its submission.

**Conflict of interest:** The authors state no conflict of interest.

# References

[1] Gkountas AA, Stamatelos AM, Kalfas AI. Recuperators investigation for high temperature supercritical carbon dioxide power generation cycles. Appl Therm Eng. 2017;125:1094–102.
[2] Chai L, Tassou SA. A review of printed circuit heat exchangers for helium and supercritical $CO_2$ Brayton cycles. Therm Sci Eng Prog. 2020;18:100543.
[3] Kim DE, Kim MH, Cha JE, Kim SO. Numerical investigation on thermal–hydraulic performance of new printed circuit heat exchanger model. Nucl Eng Des. 2008;238(12):3269–76.
[4] Wang K, He YL, Zhu HH. Integration between supercritical $CO_2$ Brayton cycles and molten salt solar power towers: A review and a comprehensive comparison of different cycle layouts. Appl Energy. 2017;195:819–36.
[5] Fan YL, Luo LG. Recent applications of advances in microchannel heat exchangers and multi-scale design optimization. Heat Transf Eng. 2008;29(5):461–74.
[6] Zheng D, Wang J, Chen ZX, Baleta J, Sundén B. Performance analysis of a plate heat exchanger using various nanofluids. Int J Heat Mass Tran. 2020;158:119993.
[7] Aneesh AM, Sharma A, Srivastava A, Chaudhury P. Effects of wavy channel configurations on thermal-hydraulic characteristics of printed circuit heat exchanger (PCHE). Int J Heat Mass Tran. 2018;118:304–15.
[8] Tsuzuki N, Kato Y, Ishiduka T. High performance printed circuit heat exchanger. Appl Therm Eng. 2007;27(10):1702–7.
[9] Chen ZX, Zheng D, Wang J, Chen L, Sundén B. Experimental investigation on heat transfer characteristics of various nanofluids in an indoor electric heater. Renew Energ. 2020;147:1011–8.
[10] Wang J, Li GL, Li T, Zeng M, Sundén B. Effect of various surfactants on stability and thermophysical properties of nanofluids. J Therm Anal Calorim. 2021;143(6):4057–70.
[11] Kim TH, Kwon JG, Yoon SH, Park HS, Kim MH, Cha JE. Numerical analysis of air-foil shaped fin performance in printed circuit heat exchanger in a supercritical carbon dioxide power cycle. Nucl Eng Des. 2015;288:110–8.
[12] Xu XY, Wang QW, Li L, Ekkad SV, Ma T. Thermal-Hydraulic Performance of Different Discontinuous Fins Used in a Printed Circuit Heat Exchanger for Supercritical $CO_2$. Numer Heat Tr A-Appl. 2015;68(10):1067–86.
[13] Chu WX, Bennett K, Cheng J, Chen YT, Wang QW. Thermo-hydraulic performance of printed circuit heat exchanger with different cambered airfoil fins. Heat Transf Eng. 2020;41(8):708–22.
[14] Cui X, Guo J, Huai X, Cheng K, Zhang H, Xiang M. Numerical study on novel airfoil fins for printed circuit heat exchanger using supercritical $CO_2$. Int J Heat Mass Transf. 2018;121:354–66.
[15] Wu JX, Xiao JB. Numerical study of crossed airfoil fins in a printed circuit heat exchanger. Appl Therm Eng. 2023;230:120646.
[16] Xi K, Zhao X, Xie ZH, Meng FK, Lu ZQ, Ji XK. Thermal-hydraulic characteristics of carbon dioxide in printed circuit heat exchangers with staggered airfoil fins. Processes. 2023;11(8):2244.
[17] Wang W, Ding L, Han F, Shuai Y, Li B, Sunden B. Parametric study on thermo-hydraulic performance of NACA airfoil fin PCHEs Channels. Energies. 2022;15(14):5095.
[18] Jiang T, Li MJ, Yang JQ. Research on optimization of structural parameters for airfoil fin PCHE based on machine learning. Appl Therm Eng. 2023;229:120498.
[19] Arora O, Cosials KF, Vaghetto R, Hassan YA. Pressure drop and friction factor study for an airfoil-fin printed circuit heat exchanger using experimental and numerical techniques. Int J Heat Fluid Flow. 2023;101:109137.
[20] Xu XY, Ma T, Li L, Zeng M, Chen YT, Huang YP, et al. Optimization of fin arrangement and channel configuration in an airfoil fin PCHE for supercritical $CO_2$ cycle. Appl Therm Eng. 2014;70(1):867–75.
[21] Huang S, Hu Y, Wang Y. Research on aerodynamic performance of a novel dolphin head-shaped bionic airfoil. Energy. 2021;214:118179.
[22] Sagong W, Jeon WP, Choi H. Hydrodynamic characteristics of the sailfish (Istiophorus platypterus) and swordfish (Xiphias gladius) in gliding postures at their cruise speeds. PLoS one. 2013;8(12):e81323.
[23] Fierstine H. An Atlantic blue marlin, Makaira nigricans, impaled by two species of billfishes (Teleostei: Istiophoridae). Bull Mar Sci. 1997;(61):495–9.
[24] Shi HY, Li MJ, Wang WQ, Qiu Y, Tao WQ. Heat transfer and friction of molten salt and supercritical $CO_2$ flowing in an airfoil channel of a printed circuit heat exchanger. Int J Heat Mass Transf. 2020;150:119006.
[25] Kwon JG, Kim TH, Park HS, Cha JE, Kim MH. Optimization of airfoil-type PCHE for the recuperator of small scale Brayton cycle by cost-based objective function. Nucl Eng Des. 2016;298:192–200.
[26] Chung S, Lee SW, Kim N, Shin SM, Kim MH, Jo H. Experimental study of printed-circuit heat exchangers with airfoil and straight channels for optimized recuperators in nitrogen Brayton cycle. Appl Therm Eng. 2023;218:119348.
[27] Chen MH, Sun XD, Christensen RN, Shi S, Skavdahl I, Utgikar V, et al. Experimental and numerical study of a printed circuit heat exchanger. Ann Nucl Energy. 2016;97:221–31.
[28] Xu XY, Ma T, Li L, Zeng M, Chen YT, Huang YP, et al. Optimization of fin arrangement and channel configuration in an airfoil fin PCHE for supercritical $CO_2$ cycle. Appl Therm Eng. 2014;70(1):867–75.